Torque and Variable Stiffness Control for Antagonistically Driven Pneumatic Muscle Actuators via a Stable Force Feedback Controller

Barkan Ugurlu, Paolo Forni, Corinne Doppmann, and Jun Morimoto

Abstract— **This paper describes a novel controller that is capable of simultaneously controlling torque and variable stiffness in real-time, for actuators with antagonistically driven pneumatic artificial muscles (PAMs). To this end, two contributions are presented: i) A stable force feedback controller that can cope with inherent PAM nonlinearities is synthesized using the dissipativity theory, for each PAM unit. ii) On top of this force feedback controller, a mathematical formulation is developed to compute reference force inputs that correspond to desired joint torque and joint stiffness inputs, concerning both agonist and antagonist PAMs. This strategy enables us to introduce real-time sensory feedback; torque and stiffness control is addressed by means of PAM force feedback control with guaranteed stability. To validate the proposed control scheme, a series of experiments were conducted on an experimental setup. As the result, the controller exhibited favorable torque and stiffness tracking in real-time, demonstrating that it could meet the performance criteria to power exoskeleton systems.**

I. Introduction

Major advances in mechatronics establish a solid basis to promote robot-assisted techniques for physiotherapy and neurorehabilitation. In particular, wearable robotic exoskeletons have potentials to be utilized both as a diagnostic tool to evaluate various key motor impairments and as a therapeutic tool to implement active assistive therapy [1]. Considering these evidences, we are in the process of developing a whole body exoskeleton system to study various research topics on robot-aided rehabilitation and sensorimotor learning.

As wearable robots do interact with human subjects in a continuous manner, torque control and physical compliance are of importance when assessing dependability, low mechanical impedance and inherent safety [2], [3]. In addition to these factors, adjustable compliance is proven to be an essential feature in human nature to stabilize arm motion when subject to disturbances [4] and to create favorable mechanical energetics via impedance matching [5]. Therefore, variable stiffness appears to be a crucial property for robotic exoskeletons, in addition to torque control.

In developing an actuation module that is capable of simultaneously controlling torque and variable stiffness, an antagonistic pair of PAMs (Pneumatic Artificial Muscle) may possess favorable characteristics, due to their superior power-to-weight ratios and physical compliance. Moreover, PAMs can be connected to joints without any heavy and high frictional mechanism, making the overall system relatively light, wearable and yet powerful [6]. Despite PAMs suffer from certain shortcomings, e.g., inherent nonlinearities, constant need of pressurized air, they were proven to be useful actuators for exoskeleton systems [7], [8].

With respect to real-time control of PAMs, Tsagarakis and Caldwell implemented a torque tracking controller with a software-controlled virtual impedance scheme [7]. Noritsugu et al. addressed hybrid position and force control with a feedforward compensator [9]. Sardellitti et al. utilized a technique to regulate stiffness via a sliding mode force controller, applied to an average PAM-valve model [10]. Vanderborght et al. implemented variable stiffness for a pleated PAM-powered biped robot, via the summation of pressure gauges [11].

In the light of these advancements, this paper presents two main contributions: 1) A novel PAM force feedback controller with guaranteed stability is synthesized based on the dissipativity theory (subsection IV-B). The controller is verified to be able to cope with the inherent nonlinearities of PAMs, since conventional controllers fail to achieve this task. 2) On top of the PAM force feedback controller, a mathematical formulation is presented to compute reference PAM force inputs that correspond to desired joint torque and joint stiffness inputs (subsection IV-A). In doing so, torque and variable stiffness control can be addressed by means of force feedback control for each PAM unit, enabling us to introduce real-time sensory feedback with guaranteed stability. In addition, real-time system performance is thoroughly tested and evaluated with a series of experiments, conducted on an actual actuator module (section V).

The paper is organized as follows. The physical setup used in the experiments is introduced in section II. PAM modeling and identification procedures are disclosed in section III. Real-time torque and variable stiffness control strategy is explained in section IV, with the related force feedback control stability proof. Experimental results are presented in section V. The paper is concluded in section VI.

II. Experimental Setup

Prior to the implementation in our multi-DoF exoskeleton, an actuator module was constructed to thoroughly test the controller's experimental performance. The module includes two antagonistically driven PAMs (Festo MAS-40) with servo pressure valves (NORGREN, VP5010SBJ series, 0-8

The authors are with the Department of Brain Robot Interface, Computational Neuroscience Laboratories, Advanced Telecommunications Research Institute International (ATR), 619-0288 Kyoto, Japan. e-mail: xmorimo@atr.jp

B. Ugurlu is also with the Department of Mechanical Engineering, Ozyegin University, 34794 Istanbul, Turkey. e-mail: barkan.ugurlu@ozyegin.edu.tr

P. Forni is also with the Department of Electrical Engineering, Imperial College London, London SW7 2BT, U.K.

C. Doppmann is also with the Department of Microengineering, Ecole Polytechnique Federale de Lausanne (EPFL), 1015 Lausanne, Switzerland.

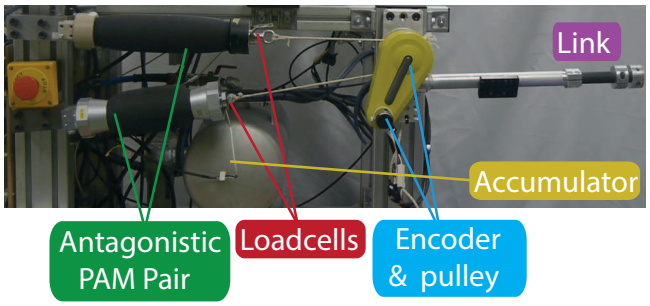

Fig. 1. The physical experimental setup [12]. Pressure servo valves are placed at the bottom, and therefore, not displayed.

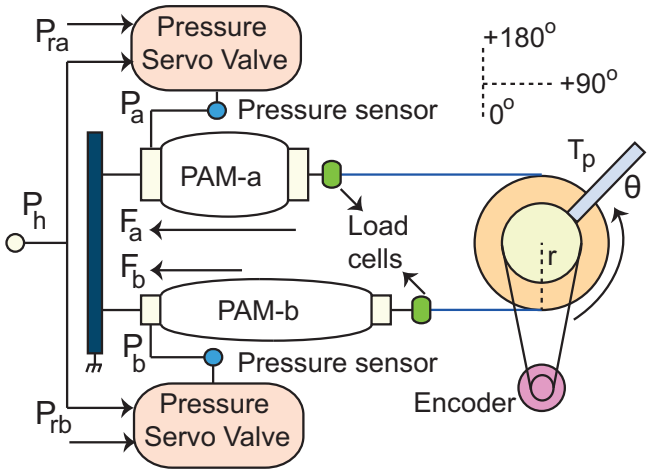

Fig. 2. Principle elements of the experimental setup.

[bar]) that control inner pressure proportional to the voltage inputs. Servo valves can also output pressure measurements. PAMs are connected via a pulley-cable system, combined with an encoder to measure the joint angle. The maximum actuator output produced via PAMs is ±70 [Nm]. Fig. 1 displays the physical system, while Fig. 2 presents its principle elements. In Fig. 2, F_a, F_b are measured PAM forces (load cell outputs), P_a, P_b are measured pressure values, P_{ra}, P_{rb} are reference pressure values, T_p is the output torque produced by PAMs, r is the pulley radius, θ is the joint angle, P_h is the supply pressure.

III. Modeling and Identification

In order to successfully implement real-time force feedback control, accurate PAM force-pressure modeling is of importance. To this end, Chou and Hannaford derived a model that is based on conservation of mechanical energy [13]. However, this method could not encapsulate the elasticity effect. Tackling this issue, Hildebrandt et al. utilized an additional 3^{rd} order polynomial function with a fractional power function, in a way to incorporate nonlinear elasticity characteristics [14]. While their model captures an important portion of PAM force-pressure-length characteristics, it may not fully represent dynamic and static frictional forces. The importance of these effects are underlined by Tondu in [15], where he uses Hill's principle to model frictional effects, without considering the models proposed in [13] and [14]. Performing an exhaustive benchmarking on the actual system, the best modeling option appears to be the superposition of [13]–[15] with minor modifications.

$$\begin{aligned} F(P,L,\dot{L}) &= P\sum_{q=0}^{2}\mu_q L^q - \left(\sum_{j=0}^{4}\eta_j L^j + \eta_5 L^{\frac{2}{3}}\right) \\ &- \operatorname{sgn}(\dot{L})\left(\sum_{k=0}^{2}\lambda_k \dot{L}^k + \lambda_3 e^{-\frac{|\dot{L}|}{\lambda_4}}\right) \quad (1) \\ F &= P\beta - \gamma \quad (2) \end{aligned}$$

In (1), F, P, L and $\dot{L}$ respectively denote force, pressure, length and length rate change of a given PAM. $\beta = \beta(L)$ and $\gamma = \gamma(L,\dot{L})$ are used to shorten expressions. Utilizing this model, both energy conservation (first term in (1)), nonlinear elasticity (second term in (1)), and frictional effects (third term in (1)) are encapsulated. Subsequently, a parameter identification procedure is executed to obtain 14 constants in (1), namely, μ_q (q=0..2), η_j (j=0..5), λ_k (k=0..4).

For this purpose, pressure inputs with varying amplitudes (up to the maximum of 8.0 [bar]) were implemented to PAMs. Input frequency was varied between 0.0 [Hz] and 4 [Hz]. In this setup, servo pressure tracking may not be possible with frequencies larger than 4 [Hz]. Load cells (see Fig. 1 and Fig. 2) were utilized to collect actual force measurements. Individual muscle lengths, (L_a, L_b), were computed via the measured joint angle;

$$L_a = L_{0a} + r(\theta - \theta_0); \qquad L_b = L_{0b} - r(\theta - \theta_0), \qquad (3)$$

in which L_{0a} and L_{0b} are PAM lengths when $\theta = \theta_0$. As the muscle co-contracted with respect to pressure inputs, disturbance forces were externally applied to the link in a random fashion, so as to enrich the data set. For each muscle, one training data set and three test data sets were collected.

Using the training data set, parameter identification was performed via a nonlinear least square fitting method. Identified parameters were placed in eq. (1) and assessed via test data sets. Fig. 3 depicts force modeling error (the difference between actual measurement and model-based computation) percentage with respect to pressure and normalized length, in the case of PAM-a. It was normalized by considering the actual force range. Similar results were obtained for PAM-b as well. Observing this figure, the maximum modeling error percentage indicates a trend between ±3%. Thus, we are able to obtain a sufficiently precise PAM model via the combination of models proposed in [13]–[15].

IV. Torque and Variable Stiffness Control

Fig. 4 displays the proposed control scheme. In this figure, T_{pr} and K_r stand for reference joint torque and joint stiffness inputs. F_{ri}, F_i, F_{ci}, P_{ri}, P_i respectively denote reference force input, actual force measurement (load cell output),

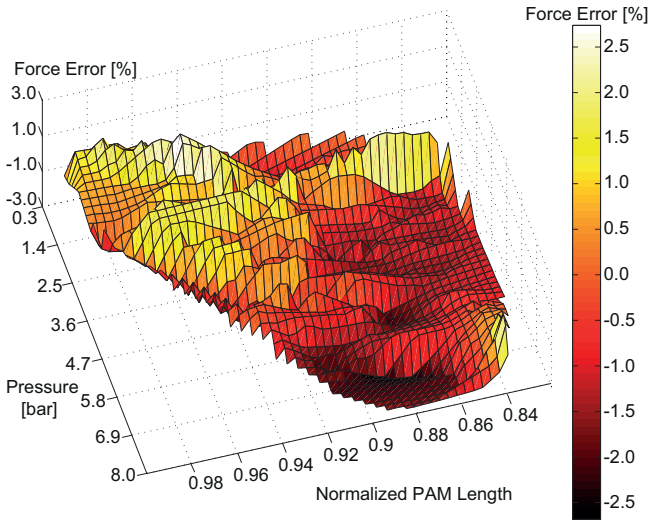

Fig. 3. PAM-a, dynamic force modeling error with respect to PAM pressure and length. Similar results were obtained for PAM-b as well.

force command (PAM force controller output), reference pressure input, and actual pressure measurement, all for the i^{th} PAM; $(i = a, b)$.

In principle, our approach can be divided into three phases: i) Computation of reference PAM force inputs (concerning both agonist and antagonist PAMs) for a given set of reference joint torque and joint stiffness inputs (subsection IV-A). ii) Implementation of stable force feedback control for individual PAMs to ensure the realization of desired joint torque and stiffness commands (subsection IV-B). iii) Pressure servo control using NORGREN valves (see Fig. 4). We mainly investigate first two phases, since the pressure control performance is ensured by the servo valves.

A. From Joint Torque&Stiffness to PAM Force References

As previously explained, we need to compute reference PAM force inputs (F_{ra}, F_{rb}) that correspond to reference torque and variable stiffness inputs (T_{pr}, K_r), so that torque and stiffness control can be addressed by means of force control for each PAM unit. With this in mind, the reference joint torque that can be generated by antagonistically paired PAMs may be obtained in terms of reference PAM forces, as indicated below (see Fig. 2).

$$T_{pr} = r\left(F_{ra} - F_{rb}\right) \tag{4}$$

Reference joint stiffness, K_r, can be derived by the partial differentiation of (4) with respect to joint angle, θ.

$$K_r = \frac{\partial T_{pr}}{\partial \theta} = r\left(\frac{\partial F_{ra}}{\partial L_a}\frac{\partial L_a}{\partial \theta} - \frac{\partial F_{rb}}{\partial L_b}\frac{\partial L_b}{\partial \theta}\right) \tag{5}$$

Applying the chain rule in (5), and acquiring $\frac{\partial L_a}{\partial \theta} = r$ and $\frac{\partial L_b}{\partial \theta} = -r$ via eq. (3), the final expression is formed in the following manner.

$$K_r = r^2\left(\frac{\partial F_{ra}}{\partial L_a} + \frac{\partial F_{rb}}{\partial L_b}\right) \tag{6}$$

Assessing (6), one needs to differentiate force equations (eq. (1)) with respect to PAM lengths for each PAM unit.

$$\begin{aligned}
F_{ra} &= P_{ra}\sum_{q=0}^{2}\mu_{qa}L_a^q - \sum_{j=0}^{4}\eta_{ja}L_a^j - \eta_{5a}L_a^{\frac{2}{3}} \\
&- \operatorname{sgn}(\dot{L}_a)\left(\sum_{k=0}^{2}\lambda_{ka}\dot{L}_a^k + \lambda_{3a}e^{-\frac{|\dot{L}_a|}{\lambda_{4a}}}\right) && (7)\\
&= P_{ra}\beta_a - \gamma_a && (8)\\
\frac{\partial F_{ra}}{\partial L_a} &= P_{ra}\sum_{q=1}^{2}q\mu_{qa}L_a^{q-1} + \frac{\partial P_{ra}}{\partial L_a}\beta_a \\
&- \sum_{j=1}^{4}j\eta_{ja}L_a^{j-1} - \frac{2}{3}\eta_{5a}L_a^{-\frac{1}{3}} && (9)\\
&= P_{ra}\Phi_a + \frac{\partial P_{ra}}{\partial L_a}\beta_a - \Psi_a && (10)\\
F_{rb} &= P_{rb}\sum_{q=0}^{2}\mu_{qb}L_b^q - \sum_{j=0}^{4}\eta_{jb}L_b^j - \eta_{5b}L_b^{\frac{2}{3}} \\
&- \operatorname{sgn}(\dot{L}_b)\left(\sum_{k=0}^{2}\lambda_{kb}\dot{L}_b^k + \lambda_{3b}e^{-\frac{|\dot{L}_b|}{\lambda_{4b}}}\right) && (11)\\
&= P_{rb}\beta_b - \gamma_b && (12)\\
\frac{\partial F_{rb}}{\partial L_b} &= P_{rb}\sum_{q=1}^{2}q\mu_{qb}L_b^{q-1} + \frac{\partial P_{rb}}{\partial L_b}\beta_b \\
&- \sum_{j=1}^{4}j\eta_{jb}L_b^{j-1} - \frac{2}{3}\eta_{5b}L_b^{-\frac{1}{3}} && (13)\\
&= P_{rb}\Phi_b + \frac{\partial P_{rb}}{\partial L_b}\beta_b - \Psi_b && (14)
\end{aligned}$$

In (7), (9), (11) and (13), (μ_{qa}, μ_{qb}) (q=0..2), (η_{ja}, η_{jb}) (j=0..5) and (λ_{ka}, λ_{kb}) (k=0..4) are PAM model parameters and identified for each muscle as previously explained in section III. β_i, γ_i, Φ_i and Ψ_i (i=a, b) are used to shorten expressions.

Furthermore, $\frac{\partial P_{ra}}{\partial L_a}$ and $\frac{\partial P_{rb}}{\partial L_b}$ are derived via the ideal gas law.

$$\frac{\partial P_{ra}}{\partial L_a} = \frac{\zeta - P_{ra}}{V_a}\frac{\partial V_a}{\partial L_a}; \quad \frac{\partial P_{rb}}{\partial L_b} = \frac{\zeta - P_{rb}}{V_b}\frac{\partial V_b}{\partial L_b}. \tag{15}$$

PAM volume V_i $(i = a, b)$ is experimentally identified with respect to L_i, using 3^{rd} order polynomials [14]. Hence, V_i and $\frac{\partial V_i}{\partial L_i}$ can be obtained. ζ is a constant specific to dry air. Refer to the Appendix to see the derivation of (15). Finally, combining (8), (12), (10), (14) and (15) in (6), the reference joint stiffness, K_r, can be expressed in terms of F_{ra} and F_{rb}.

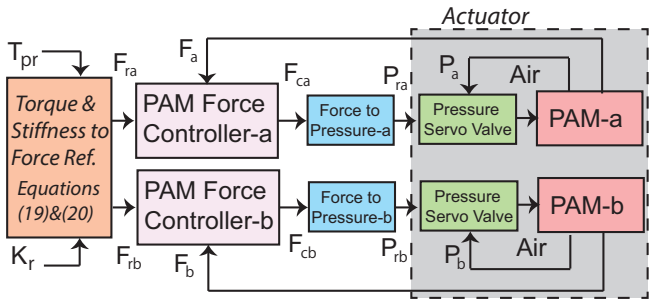

Fig. 4. The proposed control scheme. Torque&Stiffness to Force Ref. block computes reference PAM forces in accordance with desired joint torque and stiffness commands (subsection IV-A).

$$K_r = r^2\Big(\zeta(U_a+U_b)-\Psi_b-\Psi_a + W_a(F_{ra}+\gamma_a)+W_b(F_{rb}+\gamma_b)\Big), \quad (16)$$

$$U_i = \frac{\beta_i}{V_i}\frac{\partial V_i}{\partial L_i}, \quad (17)$$

$$W_i = \frac{\Phi_i - U_i}{\beta_i}. \quad (18)$$

In (16), sub-expressions U_i and W_i (i=a,b) are used to ease the computation. Eqs. (4) and (16) constitute a set of formulae to compute joint torque and stiffness in terms of PAM forces. Since our main purpose is to obtain PAM forces in terms of joint torque and stiffness, (4) and (16) are solved to obtain PAM forces. As such, reference PAM forces may be sequentially computed as shown below.

$$F_{ra} = \frac{1}{W_a+W_b}\left(\frac{K_r}{r^2}+\Psi_b+\Psi_a-W_a\gamma_a - W_b\left(\gamma_b-\frac{T_r}{r}\right)-\zeta(U_a+U_b)\right) \quad (19)$$

$$F_{rb} = F_{ra}-\frac{T_r}{r} \quad (20)$$

B. Stable Force Feedback Control for PAMs

The stability proof for the i^{th} (i=a,b) PAM force feedback control is given by using the dissipativity theory. Refer to [16] for the mathematical background of the proof.

As displayed in Fig. 4, reference pressure inputs (P_{ri}) are inserted to pressure servo valves (NORGREN VP5010SBJ). These valves include a built-in pressure servo loop with necessary feedback control, regulating the air flow to realize the desired pressure commands. Therefore, the relation between servo valve input-output (P_i∼P_{ri}) can be expressed using a delay model [10].

$$\epsilon\dot{P}_i = -P_i + P_{ri} \quad (21)$$

ϵ is the delay constant. P_{ri} is computed by inserting the force command (PAM force controller output, F_{ci}) into the corresponding force-pressure mode, see Fig. 4. Plugging (21) into (2), the following is yielded.

$$\dot{P}_i = -\frac{P_i}{\epsilon}+\frac{F_{ci}+\gamma_i}{\epsilon\beta_i} \quad (22)$$

The force error F_{ei} is computed using reference force (F_{ri}) and actual force (F_i) as follows.

$$F_{ei} = F_{ri}-F_i = F_{ri}-(P_i\beta_i-\gamma_i) \quad (23)$$

Albeit the mapping $F_{ci}\mapsto F_{ei}$ is not passive, we can still render the plant passive with respect to the mapping $\upsilon_i \mapsto F_{ei}$, where υ is an external input to be defined. The storage function, $S(P)$, is selected as follows.

$$S(P) = \frac{1}{2}\epsilon F_{ei}^2 \quad (24)$$

Differentiating (24) yields the following.

$$\dot{S}(P) = \epsilon F_{ei}\dot{F}_{ei} = \epsilon F_{ei}(\dot{F}_{ri}-\dot{F}_i) = \epsilon F_{ei}(\dot{F}_{ri}-\dot{P}_i\beta_i-P_i\dot{\beta}_i+\dot{\gamma}_i) \quad (25)$$

If we place (22) into (25),

$$\dot{S}(P) = F_{ei}(\epsilon(\dot{F}_{ri}-P_i\dot{\beta}_i+\dot{\gamma}_i)+P_i\beta_i-\gamma_i-F_{ci})) \quad (26)$$

and recalling that $F_i = P_i\beta_i-\gamma_i$,

$$\dot{S}(P) = F_{ei}(\epsilon(\dot{F}_{ri}-P_i\dot{\beta}_i+\dot{\gamma}_i)+F_i-F_{ci}). \quad (27)$$

Command signal F_{ci} is assigned as follows.

$$F_{ci} = F_{ri}+\epsilon(\dot{F}_{ri}-P_i\dot{\beta}_i+\dot{\gamma}_i)-\upsilon_i \quad (28)$$

where υ_i is the external control input. In force command (28), $\epsilon(\dot{\gamma}_i - P_i\dot{\beta}_i)$ stands for nonlinear passifying terms, whereas $F_{ri}+\epsilon\dot{F}_{ri}$ indicate the feedforward input. Placing (28) in (27), $\dot{S}(P)$ reduces to the following.

$$\dot{S}(P) = F_{ei}(F_i-F_{ri}+\upsilon_i) = F_{ei}(-F_{ei}+\upsilon_i) \quad (29)$$

$$= -F_{ei}^2+F_{ei}\upsilon_i \le F_{ei}\upsilon_i \quad (30)$$

Therefore, (29) indicates that the plant (22)-(23), together with the F_{ci} command that includes feedforward and nonlinear passifying terms, is a strictly passive system with respect to input υ_i and output F_{ei} [16]. υ_i is constructed using a lead-lag controller with limited integral action and a low pass filter on the derivative term (see $C_i(s)$ in Fig. 5).

$$\upsilon_i = -F_{ei}C_i;\quad C_i(s) = K_{Pi}\Xi\frac{1+T_{Ii}s}{1+\Xi T_{Ii}s}\frac{1+T_{Di}s}{1+\alpha T_{Di}s} \quad (31)$$

In (31), we have $0\le T_{Di}<T_{Ii}$, $1\le\Xi<\infty$, and $0\le\alpha<1$; K_{Pi}, T_{Di}, T_{Ii} are controller gains, tuned via a Ziegler-Nichols-like approach. Fig. 5 displays the controlling strategy in which feedforward terms ($F_{ri}+\epsilon\dot{F}_{ri}$), nonlinear passifying terms ($\epsilon\dot{\gamma}_i-\epsilon P_i\dot{\beta}_i$), and feedback control action ($F_{ei}C_i$)

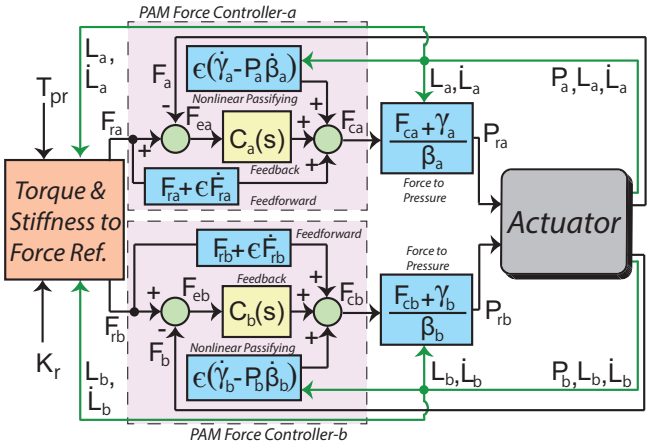

Fig. 5. The detailed control scheme in which PAM force feedback controllers are explicitly illustrated. In this controller, both feedforward terms, feedback terms, and nonlinear passifying terms are incorporated. Force measurements (F_a, F_b) are acquired via load cells. Encoder readings are used to compute real-time PAM lengths (L_a, L_b).

are incorporated in accordance with (28), the outcome of the stability analysis. Here, the plant with the precompensator (combination of feedforward and nonlinear passifying terms) and the controller constitute a system with passive feedback interconnections. Utilizing the direct implication given in (30), the system is asymptotically stable and Bounded-Input-Bounded-Output stable [16].

Synthesizing the controller in this manner not only provides a mathematical proof to guarantee stability, but also ensures a high tracking performance thanks to nonlinear passifying and feedforward terms. The controller compensates certain nonlinearities that are inherent to PAM actuators, enabling our feedback controller to perform well. In practice, we confirmed that solely implementing the classical feedback controllers (PID or lead-lag only, without nonlinear passifying and feedforward terms) resulted with unacceptable tracking performance and often led to instability. Conventionally implemented PID with feedforward approach (PID + F_{ri}) may provide tracking; however, its performance is observed to be not as satisfactory. Moreover, stability may not be guaranteed for these alternatives.

V. Experiment Results

To validate the proposed control frame, a series of experiments were conducted on the actuator module that is described in section II. Results are given in Figs. 6-8. Fig. 6 displays stand-alone torque tracking results. Fig. 7 and Fig. 8 display simultaneous torque and variable stiffness tracking results. Due to safety precautions, torque input amplitudes were kept within certain limits. In Figs. 6-8, dotted blue, solid cyan, dotted purple, solid green, dotted pink and solid orange lines indicate reference torque, measured torque, reference stiffness, estimated stiffness, reference agonist PAM force and measured agonist PAM force variations, respectively.

To examine the torque tracking performances for static or slowly-varying inputs, a gravity compensation task was implemented. Its result is given in Fig. 6(a). Yellow hatched areas show the periods in which the tip weight was statically balanced by the controller (i, ii, v) or followed the commands of a slowly-varying external manipulation. (iii, iv). Pink areas stand for transitions between the postures. Note that the controller strictly provides the overall torque to cancel out the gravitational load. In this task, a tip weight of 7.5 [kg] dumbbell was attached to the actuator link (0.9 [kg]) and it maintained its posture regardless of the joint position. Refer to the multimedia attachment to view scenes from gravity compensation experiments with different tip weights.

Fig. 6(b) and Fig. 6(c) show relatively slow and fast torque reference tracking for sine wave inputs at 0.5 [Hz], and at 3.0 [Hz], respectively. In both cases, the controller showed satisfactory tracking performances in which tracking delays were negligible for practical applications. Although a frequency domain analysis indicated that the controller can track torque inputs up to 4 [Hz], the inputs faster than 3.2 [Hz] were found to be infeasible as the delay largely grows.

Fig. 7(a) and Fig. 7(b) depict results from a simultaneous torque and variable stiffness tracking experiment. Torque reference was assigned via a sine wave signal with a frequency at 2.2 [Hz] and with a peak-to-peak amplitude of $\pm$15 [Nm]. Stiffness reference was given via a sine wave with a frequency at 0.37 [Hz] and with a peak-to-peak amplitude of 60$\pm$15 [Nm/rad]. As the result, simultaneous torque and stiffness tracking control was achieved, despite the fact that both inputs had distinct frequencies. In this case, torque input frequency was greater than stiffness input frequency; 2.2 [Hz] $>$ 0.37 [Hz]. This result indicated that the proposed controller can reliably achieve simultaneous torque and variable stiffness control.

As explained in section IV, eqs. (19) and (20) are used to compute reference force inputs that correspond to desired torque and stiffness inputs, concerning both agonist and antagonist muscles. Thus, torque and stiffness control is addressed by means of stabilized force feedback control. In Fig. 7(c), reference and measured force variations for the agonist muscle (PAM-a) were plotted. It can be observed that the reference PAM-a force reference appeared to be an interference pattern of two distinct frequencies, introduced by torque (2.2 [Hz]) and stiffness (0.37 [Hz]) inputs. This interference signal was well tracked thanks to the stabilized force feedback control strategy, introduced in Fig. 5. A similar result was obtained for the antagonist muscle (PAM-b), thus not plotted.

Fig. 8(a) and Fig. 8(b) show torque and stiffness tracking results from another experiment in which torque input frequency was 0.5 [Hz] and stiffness input frequency was 2.0 [Hz]. In contrast to the previous case, stiffness input frequency was greater than torque input frequency; 2.0 [Hz] $>$ 0.5 [Hz]. Amplitudes were kept the same as in Fig. 7. Tracking performances were quite satisfactory; regardless of the differences in torque and stiffness input frequencies, the controller achieved simultaneous torque-stiffness tracking control. Similarly, the force reference in Fig. 8(c) for the agonist PAM appeared to be an interference pattern of two

distinct input frequencies, so that it could satisfy both constraints. This force reference was also well tracked, thanks to the proposed force feedback control. A similar result was obtained for PAM-b, thus not plotted.

VI. Conclusion

We proposed a novel PAM force feedback controller with guaranteed stability, synthesized via the dissipativity theory. On top of this force feedback controller, a mathematical formulation was developed to compute reference PAM force inputs for a given set of desired joint torque and joint stiffness inputs. Therefore, torque and variable stiffness control was addressed by means of force feedback control for each PAM unit, enabling us to introduce real-time sensory feedback with guaranteed stability. A series of experiment results were presented to validate the performance of simultaneous torque and stiffness tracking control.

In Fig. 7 and Fig. 8, the tracking performances in lower frequencies may suffer from inevitable harmonics with sufficiently small amplitudes, although this issue was not observed to be a drawback in our applications [17]. When applying inputs with distinct frequencies to a multi-input-multi-output system, the faster input may cause such effects, as in this case.

In general, PAMs may not perform tracking as favorable as electrical motors, due to the fact that air flow is much slower than electrical current. As a result, the control bandwidth is narrower because of the inevitable delays in the air pressure servo loop. On the contrary, electrically actuated systems may not allow the simultaneous control of torque and stiffness unless complicated mechanisms are designed [6]. They are also heavier and intrinsically not compliant.

On this matter, we highlight the fact that we do not intend to make bold comparison statements; one should choose the actuator type depending on the system requirements. In our case, we aimed for a powerful and light system with physical compliance, and thus, chose pneumatic muscles. In this respect, this paper is written to report the way we handle the problem of stabilized PAM control, as the proposed scheme satisfactorily met the performance objectives.

Multi-DoF application of this work is straightforward, as the method provides a reliable torque and stiffness control strategy with guaranteed stability. Indeed, we successfully built balance recovery controllers on top of the proposed scheme, for a lower body exoskeleton that is powered via identical PAMs, see [17]. Therefore, our next report will be concerning the exploitation of variable stiffness control for sensorimotor learning and robot-assisted rehabilitation.

Appendix - Derivation of $\frac{\partial P}{\partial L}$ for Dry Air at 5 ^oC

A compressed air dryer provides dry air for our pneumatic actuators at a constant temperature of 5 ^oC. Using the chain rule, partial differentiation of the PAM pressure (P) with respect to PAM length (L) is expressed below.

$$\frac{\partial P}{\partial L} = \frac{\partial P}{\partial V}\frac{\partial V}{\partial L} \tag{32}$$

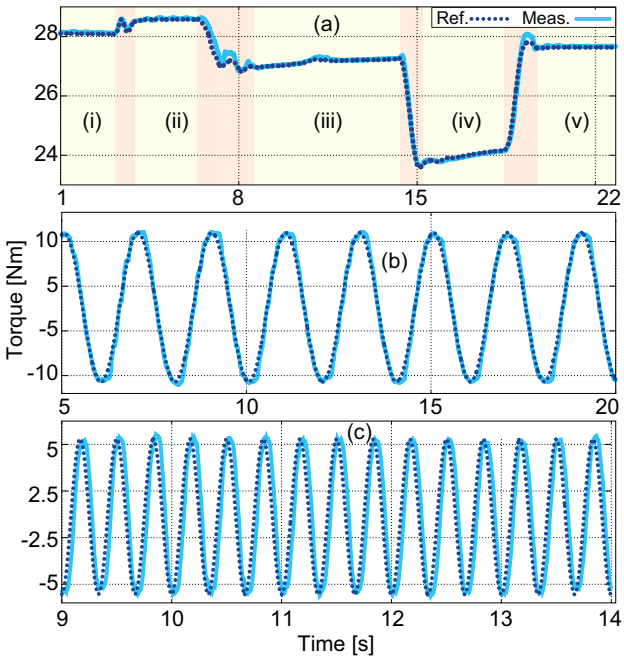

Fig. 6. Torque tracking for distinct inputs. a) Gravity compensation task. b) Sine wave input at 0.5 [Hz]. b) Sine wave input at 3.0 [Hz].

PAM volume V can be experimentally characterized in terms of L, using a 3^{rd} order polynomial [14]. Therefore, $\frac{\partial V}{\partial L}$ can be computed. As we now need to formulate $\frac{\partial P}{\partial V}$, the ideal gas law for constant temperature (T) is used.

$$PV = mR_{sp}T \tag{33}$$

In (33), m and R_{sp}, respectively refer to gas mass, and specific gas constant for dry air at 5 ^oC. Differentiating both sides of (33) with respect to V, the following is yielded.

$$\frac{\partial}{\partial V}(PV) = \frac{\partial m}{\partial V}R_{sp}T \tag{34}$$

$$P + \frac{\partial P}{\partial V}V = \rho R_{sp}T \tag{35}$$

In (35), ρ is the density of dry air. At 5 ^oC (T=278.15 K), ρ and R_{sp} are 1.269 [kgm^{-3}] and 278.058 [Nm$kg^{-1}K^{-1}$]. Despite the fact that ρ may change depending on the pressure, we consider it constant to prevent complicated modeling. Compared to the conventional approach in which $\frac{\partial P}{\partial L}$ is totally omitted, our approach is physically more consistent. To have a simpler notation, $\rho R_{sp}T$ constant is called ζ. Using (35), $\frac{\partial P}{\partial V}$ can be yielded. Plugging it into (32), the final derivation is completed as below.

$$\frac{\partial P}{\partial L} = \frac{(\zeta - P)}{V}\frac{\partial V}{\partial L} \tag{36}$$

Acknowledgment

This research was supported by MEXT KAKENHI 23120004, SRPBS from MEXT/AMED, ImPACT Program

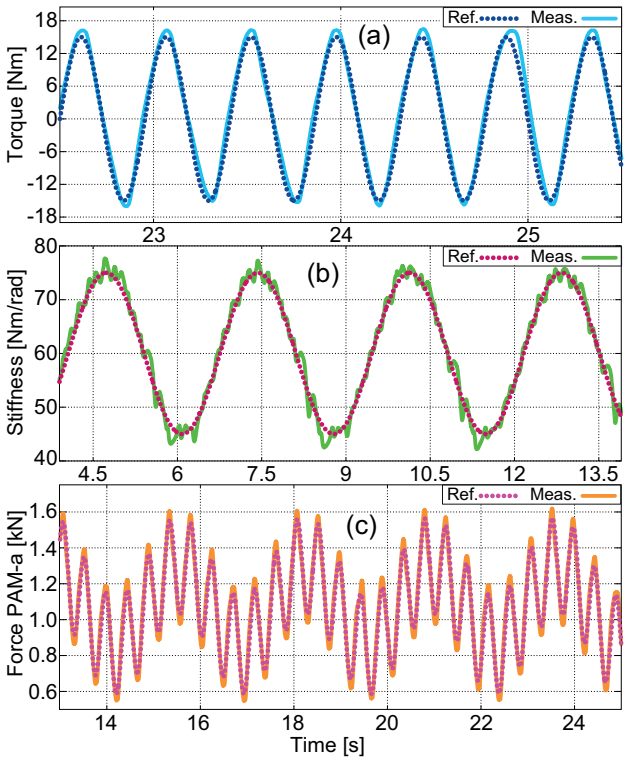

Fig. 7. a) Torque tracking results for a sine wave input at 2.2 [Hz]. b) Stiffness tracking results for a sine wave input at 0.37 [Hz]. c) Agonist muscle (PAM-a) force tracking.

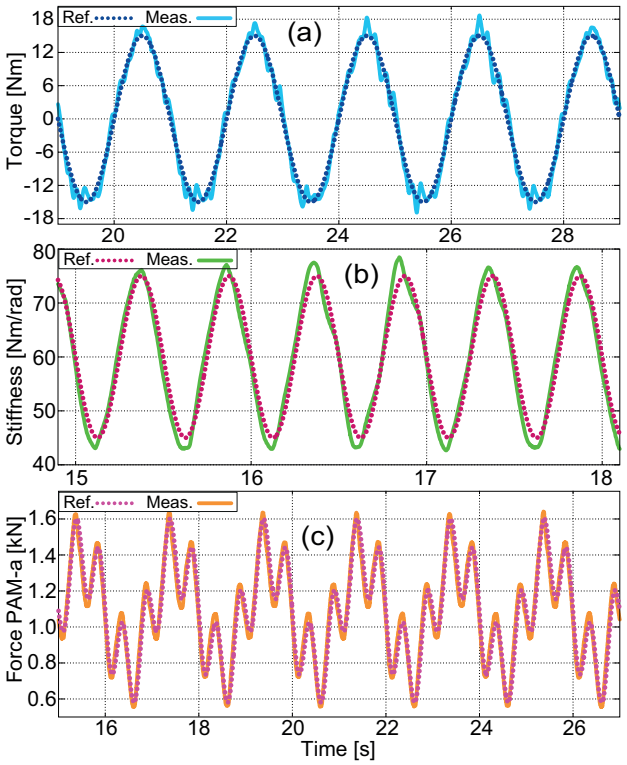

Fig. 8. a) Torque tracking results for a sine wave input at 0.5 [Hz]. b) Stiffness tracking results for a sine wave input at 2.0 [Hz]. c) Agonist muscle (PAM-a) force tracking.

of Council for Science, Technology and Innovation (Cabinet Office, Government of Japan), "Development of Medical Devices and Systems for Advanced Medical Services" from NEDO/AMED, MIC-SCOPE. The authors thank T. Teramae and T. Noda for the development of the experimental setup.

REFERENCES

[1] D. J. Reinkensmeyer, L. E. Kahn, M. Averbuch, A. McKenna-Cole, B. D. Schmit, and W. Z. Rymer, "Understanding and treating arm movement impairment after chronic brain injury: Progress with arm guide," in *Journal of Rehabilitation Research and Development*, vol. 37, no. 6, 2000, pp. 653-662.

[2] M. Zinn, O. Khatib, B. Roth, and J. K. Salisbury, "Playing it safe [human-friendly robot]," in *IEEE Robotics & Automation Magazine*, vol. 11, no. 2, 2004, pp. 12-21.

[3] A. De Santis, B. Siciliano, A. De Luca, and A. Bicchi, "An atlas of physical human-robot interaction," in *Mechanism and Machine Theory*, vol. 43, no. 3, 2008, pp. 253-270.

[4] E. Burdet, R. Osu, D. Franklin, T. E. Milner, and M. Kawato, "The central nervous system stabilizes unstable dynamics by learning optimal impedance," in *Nature*, vol. 414, 2001, pp. 446-449.

[5] W. A. Farahat, and H. Herr, "Optimal workloop energetics of muscle-actuated systems: An impedance matching view," in *PLoS Computational Biology*, vol. 6, no. 6, 2010, pp. 1-11.

[6] B. Vanderborght et al., "Variable impedance actuators: A review," in *Robotics and Autonomous Sys.*, vol. 61, no. 12, 2013, pp. 1601-1614.

[7] N. G. Tsagarakis, and D. G. Caldwell, "Development and control of a 'soft-actuated' exoskeleton for use in physiotherapy and training," in *Autonomous Robots*, vol. 15, no. 1, 2003, pp. 21-33.

[8] H. Kobayashi, A. Uchimura, Y. Ishida, K. Hiramatsu, M. Konami, T. Matsushita, and Y. Sato, "Development of a muscle suit for the upper body - realization of abduction motion," in *Advanced Robotics*, vol. 18. no. 5, 2004, pp. 497-513.

[9] T. Noritsugu, F. Ando, S. Dohta, T. Yamanaka, "Hybrid-type position and force control of robot manipulator using artificial rubber muscle," in *Journal of Robotics and Mechatronics*, vol. 7, no. 6, pp. 436-442.

[10] I. Sardellitti, G. Palli, N. G. Tsagarakis, and D. G. Caldwell, "Antagonistically actuated compliant joint: Torque and stiffness control," in *Proc. IEEE Conf. on Intelligent Robots and Systems*, Taipei, Taiwan, 2010, pp. 1909-1914.

[11] B. Vanderborght, R. Van Ham, B. Verrelst, M. Van Damme, and D. Lefeber, "Overview of the Lucy project: Dynamic stabilization of a biped powered by pneumatic artificial muscles," in *Advanced Robotics*, vol. 22, no. 10, 2008, pp. 1027-1051,

[12] T. Noda, J.-I. Furukawa, T. Teramae, S.-H. Hyon, and J. Morimoto "An electromyogram based force control coordinated in assistive interaction," in *Proc. IEEE Conf. on Robotics and Automation*, Karlsruhe, Germany, 2013, pp. 2657-2662.

[13] C.-P. Chou, and B. Hannaford, "Measurement and modeling of McKibben pneumatic artificial muscles," in *IEEE Trans. on Robotics and Automation*, vol. 12, no. 1, 1996, pp. 90-102.

[14] A. Hildebrandt, O. Sawodny, R. Neumann, and A. Hartmann, "Cascaded control concept of a robot with two degrees of freedom driven by four artificial pneumatic muscle actuators," in *Proc. IEEE Conf. on American Control Conference*, Portland, US, 2005, pp. 680-685.

[15] B. Tondu, "Closed-loop position control of artificial muscles with a single integral action: Application to robust positioning of McKibben artificial muscle," in *Proc. IEEE Conf. on Mechatronics*, Vicenza, Italy, 2013, pp. 718-723.

[16] B. Brogliato, R. Lozano, B. Maschke, and O. Egeland. *Dissipative Systems Analysis and Control: Theory and Applications.* London, U.K.: Springer, 2010.

[17] C. Doppmann, B. Ugurlu, M. Hamaya, T. Teramae, T. Noda, and J. Morimoto "Towards Balance Recovery Control for Lower Body Exoskeleton Robots with Variable Stiffness Actuators: Spring-Loaded Flywheel Model," in *Proc. IEEE Conf. on Robotics and Automation*, Seattle, US, 2015, pp. 5551-5556.